



Heriot-Watt University
Research Gateway

Experimental investigation of a triple pontoon wave energy converter and breakwater hybrid system

Citation for published version:

Peng, W, Zhang, Y, Zou, Q, Yang, X, Liu, Y & Zhang, J 2021, 'Experimental investigation of a triple pontoon wave energy converter and breakwater hybrid system', *IET Renewable Power Generation*, vol. 15, no. 14, pp. 3151-3164. <https://doi.org/10.1049/rpg2.12214>

Digital Object Identifier (DOI):

[10.1049/rpg2.12214](https://doi.org/10.1049/rpg2.12214)

Link:

[Link to publication record in Heriot-Watt Research Portal](#)

Document Version:

Publisher's PDF, also known as Version of record

Published In:

IET Renewable Power Generation

Publisher Rights Statement:

© 2021 The Authors.

General rights

Copyright for the publications made accessible via Heriot-Watt Research Portal is retained by the author(s) and / or other copyright owners and it is a condition of accessing these publications that users recognise and abide by the legal requirements associated with these rights.

Take down policy

Heriot-Watt University has made every reasonable effort to ensure that the content in Heriot-Watt Research Portal complies with UK legislation. If you believe that the public display of this file breaches copyright please contact open.access@hw.ac.uk providing details, and we will remove access to the work immediately and investigate your claim.

Experimental investigation of a triple pontoon wave energy converter and breakwater hybrid system

Wei Peng¹  | Yingnan Zhang¹ | Qingping Zou² | Xueer Yang¹ | Yanjun Liu³ | Jisheng Zhang¹

¹ Key Laboratory of Ministry of Education for Coastal Disaster and Protection, Hohai University, 1 Xikang Road, Nanjing 210024, China

² The Lyell Centre for Earth and Marine Science and Technology, Institute for Infrastructure and Environment, Heriot-Watt University, Edinburgh EH14 4AS, UK

³ School of Mechanical Engineering, Shandong University, 27 Shandan Road, Ji'nan 250100, China

Correspondence

Wei Peng, Key Laboratory of Ministry of Education for Coastal Disaster and Protection, Hohai University, 1 Xikang Road, Nanjing 210098, China.
Email: pengwei597@163.com

Funding information

National Natural Science Foundation of China, Grant/Award Numbers: U1706230, 51709095; Fundamental Research Funds for the Central Universities, Grant/Award Number: B210202028; Marine Renewable Energy Foundation, State Oceanic Administration, China, Grant/Award Number: GHME2017YY01

Abstract

In this paper, a novel hybrid wave energy converter (WEC)-floating breakwater system consisting of three floating pontoons with power take-off (PTO) modules is developed to extract wave energy from heave motion and attenuate waves to protect the coast. Unlike previous studies of this subject, the present three pontoons are in close proximity so that they may share the same foundation to reduce the cost further and both pontoons with step change drafts and same drafts are investigated. A systematic experimental study was carried out in a wave flume to examine the hydrodynamic characteristics of the hybrid system under regular waves. The experimental results are used to assess the influences of the WEC-breakwater integration and the configuration of pontoons on the hydrodynamic performance of the hybrid system as a WEC and a breakwater. It was found that the integration of multiple energy-extracting pontoons is robust in smoothing out the power output fluctuations, and the floating pontoons with same drafts gave rise to higher energy conversion efficiency while the floating pontoons with step change drafts are more effective in attenuating wave energy. A parametric analysis is able to identify the balanced performance of the system as a WEC and a breakwater.

1 | INTRODUCTION

Due to rapidly increasing global demand for energy security and CO₂ emission reduction, ocean renewable energy exploitation has attracted growing attention in recent decades, as the ocean constitutes a vast and largely untapped reservoir of energy. Among ocean renewable energy, wave energy is the most promising because of its high energy density, predictability, and widespread availability [1, 2]. As a result, a large number of wave energy converter (WEC) configurations have been proposed, and thousands of wave energy extraction techniques have been patented worldwide. Among those WECs, some have progressed significantly with promising energy conversion mechanisms, e.g. the Limpet [3], Seawave Slot-Cone Generator (SSG) [4], Powerbuoy [5] and WaveRoller [6]. Wave energy

is harvested by making use of buoy motions directly activated by the cyclic oscillation of waves and wave-induced air pressurization for oscillating buoy (OB)-type and oscillating water column (OWC)-type WECs, respectively. For overtopping devices, waves are usually focused onto a slope from which the waves overtop into a reservoir, transferring wave energy into potential energy and hence electric power. As of now, OB-type WECs have been widely studied and tested owing to their good adaptability to varied water depths and sea level changes. Since the 1970s, the performance of OB WECs has been investigated for various energy conversion methodologies by Stratigaki et al. [7], Chow et al. [8], Yang et al. [9] and Martinelli et al. [10].

However, it is well recognized that a host of challenges, including the high costs of current wave energy technologies

This is an open access article under the terms of the [Creative Commons Attribution](https://creativecommons.org/licenses/by/4.0/) License, which permits use, distribution and reproduction in any medium, provided the original work is properly cited.

© 2021 The Authors. *IET Renewable Power Generation* published by John Wiley & Sons Ltd on behalf of The Institution of Engineering and Technology

[11], have made the electricity generated by wave energy devices not economically competitive which impeded the industrial and commercial development of WECs. Recently, it was proposed that integrating WECs into coastal structures or offshore wind energy facilities is a feasible measure to reduce the cost [12–15] (see Zhao et al. [15] and Pérez-Collazo et al. [16] for a comprehensive review). For example, a reduced capital cost per megawatt installed was achieved by sharing the electrical installation and foundation in the combination of a spar-type floating wind turbine (FWT) and a torus (donut-shaped) point absorber-type WEC [17]. Nguyen and Wang [18] proposed heaving WEC-type attachments to a pontoon-type very large floating structure (VLFS) to extract wave energy and reduce the hydro-elastic response of VLFS. Palma et al. [19] proposed a multifunctional device referred to as OBREC (Overtopping Breakwater for Energy Conversion), which was aimed at producing energy from waves and protecting harbour areas from flooding at the same time. Ashlin et al. [20] conducted experiments in a shallow wave basin to investigate the effect of device spacing on the hydrodynamic performance of an array of OWC devices integrated with an offshore detached breakwater (ODBW) device. Peng et al. [21] developed a numerical model based on the Navier-Stokes solver to optimize the performance of a submerged wave energy converting device mounted on a floating breakwater. They found that a tuning strategy utilizing supplementary springs is robust in helping the device to maintain a high energy capture width for various wave conditions.

Floating breakwaters (FBs) are widely used coastal defence structures, therefore, promising marine structures for integration with WECs, as they are often deployed in similar marine environmental conditions [22, 23]. To a certain extent, FBs and WECs are functionally complementary, as both aim to decrease incident wave energy, although the former focuses on energy dissipation or reflection, while the latter emphasizes energy conversion. Therefore, WEC-FB devices have been proposed to take advantage of both the aforementioned functions. For instance, floating breakwaters with pneumatic chambers were numerically investigated by Koo [24] and experimentally studied by He et al. [25, 26]. They found that the integrated system equipped with an OWC device can improve the wave attenuation performance and possess the potential to extract wave energy. More recently, Martinelli et al. [27] proposed a hybrid structure consisting of an “active” floating breakwater coupled with a new type of wave energy converter referred to as ShoWED. Their experimental results indicate that the efficiency of ShoWED could reach up to 26% by making use of the reflected waves from the breakwater. Similarly, Ning et al. [28–30], Zhao et al. [31] and Guo et al. [32] studied an integrated system with a floating breakwater and an OB-type WEC in heave motion. It was found that the capture width ratio (CWR) of the integrated system may reach up to 24%, while the transmission coefficient was kept lower than 0.5 [28]. These studies suggest that floating breakwaters are ideal for integration with OB-type devices to achieve dual purpose of wave energy extraction and shore protection.

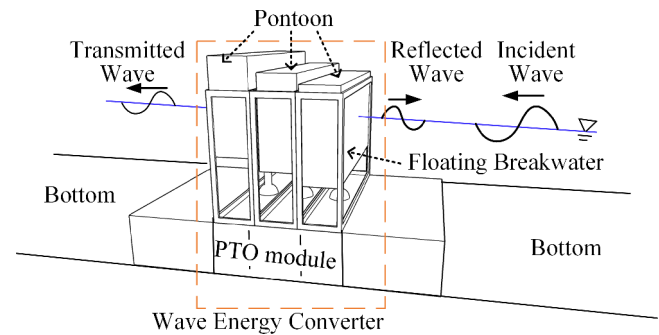


FIGURE 1 Schematic diagram of the integrated wave energy converter (orange dashed box) and floating breakwater system with triple pontoons

The present study is aimed at developing an integrated system consisting of multiple floating pontoons in close proximity with varying draft. A schematic diagram of the proposed integrated system is shown in Figure 1. The pontoons are arranged close to each other and restrained to having only one degree of freedom heave motion. Under the action of water waves, the floating pontoons heave up and down with the undulating free surface and drive the alternator to generate electricity. Compared with the hybrid device combined with a fixed breakwater, the present WEC-breakwater system has the advantages of feasibility in deep water, adaptability for poor foundation and environmental friendliness due to minimum interference with water circulation and fish migration.

Thus, the present hybrid system is favourable in practical applications because of its dual purpose for protecting coastal infrastructure, such as small craft harbours or marinas and extracting wave power at the same time. Furthermore, previous studies [15, 31, 32] have focused on WEC-breakwater with single, dual and multiple pontoons with little interactions with each other. Unlike these studies, multiple pontoons in this study are closer to each other, so that the interaction between wave and pontoons is more complicated and not well understood. The cluster of multiple pontoons share one foundation, therefore, is more cost-efficient. The multiple pontoons in this study form a breakwater front slope to attenuate wave through breaking and smooth out the variation of wave power outputs.

The objective of this paper is to investigate the combined hydrodynamic characteristics of the proposed system in extracting wave energy and attenuating wave height. To that end, a physical model was established, and the interactions of non-linear waves with the present hybrid system are analysed using the wave flume test data. Then, the wave reflection, transmission and dissipation coefficients and energy conversion efficiency of the proposed integrated system is extracted from the parametric analysis in frequency domain. The rest of the paper is organized as follows. The physical model and experimental methodology are described in Section 2. Experimental results and discussions are presented in Section 3. Finally, the conclusions of this study are summarized in Section 4.

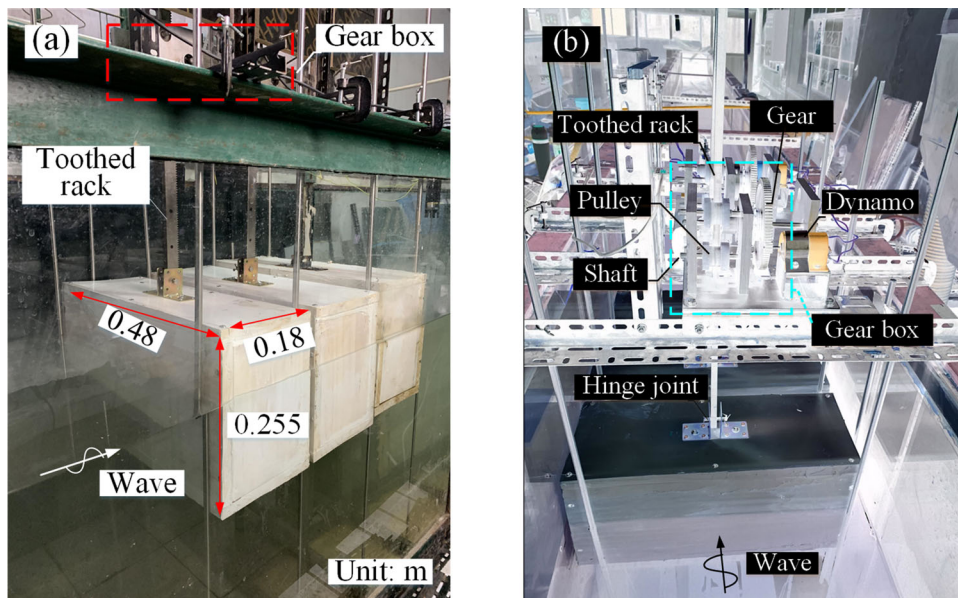


FIGURE 2 Schematic diagram of the physical model and its installation in the wave tank: (a) side view and (b) front view

2 | EXPERIMENT

2.1 | Physical model

The integrated wave energy converting system consists of three box-type floating pontoons that also function as breakwaters, working under the principle of an oscillating buoy WEC. The floating pontoons were restrained to remain close to each other, and their motions were assumed to be mainly governed by the heave motion, where the other five degrees of freedom (i.e. surge, sway, pitch, roll and yaw) motion were negligible due to the boundary condition. The spacing among the pontoons remained approximately 1 cm due to the frame installed to guarantee the vertical motion of buoys. The frame was made of stainless steel rods, and the friction between the frame and buoys was assumed to be negligible. As the main concern was the interaction of water waves with the developed wave

energy conversion system, the electricity generation module was replaced by the summation of the damping force from gear boxes and dynamos (see Figure 2) and the Ampere force from the dynamos. The gear boxes were designed, as shown in Figure 3, with a speed-up ratio of 10.00, and were then used to speed up the rotational velocity of the dynamo hub. A ratchet mechanism was used in the gear box so that the rotating direction of the dynamo hub remained the same during the experiment. The applied dynamos were kept at the rate of 5.00 V and 3.00 W. According to the dimensions of the experimental facilities and tested wave conditions, a geometrical similarity scale of 1:10 was used for the model test. More specifically, Figure 2 shows the physical model of the pontoon and its size. Along the wave propagation direction, three identically sized pontoons were deployed, with only the front two pontoons were installed with energy extraction modules, as illustrated in Figure 4.

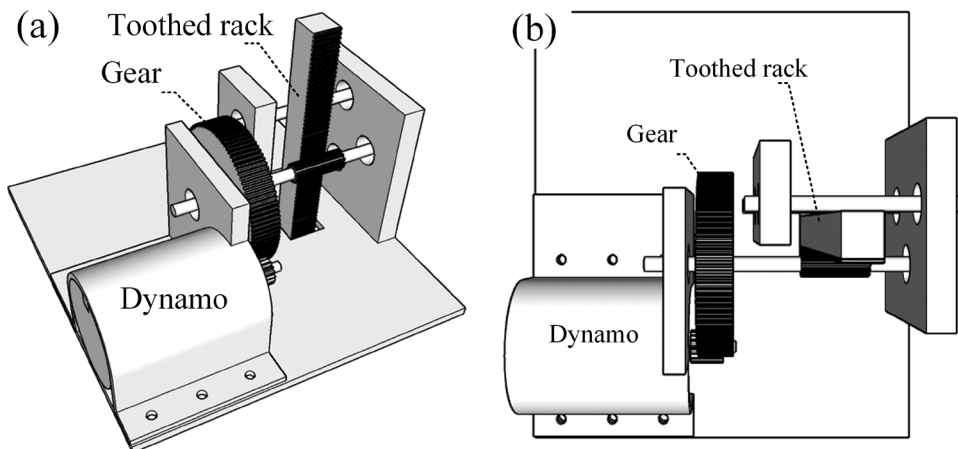


FIGURE 3 Schematic diagram of the electro-mechanical gear box: (a) side view and (b) top view

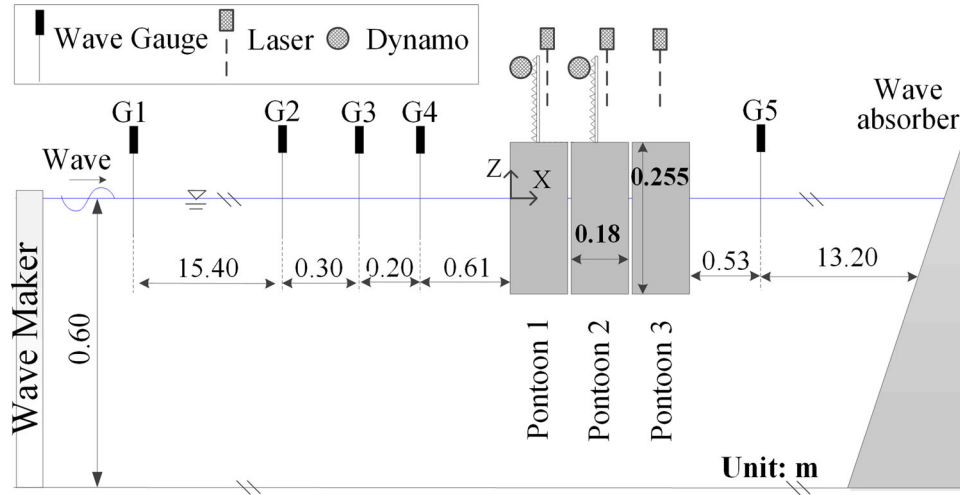


FIGURE 4 A sketch of the experiment setup of WEC-floating breakwater system with triple pontoons in a 2-D wave flume with all dimensions in m and locations of wave gauges G1–G5, three laser sensors and two dynamos

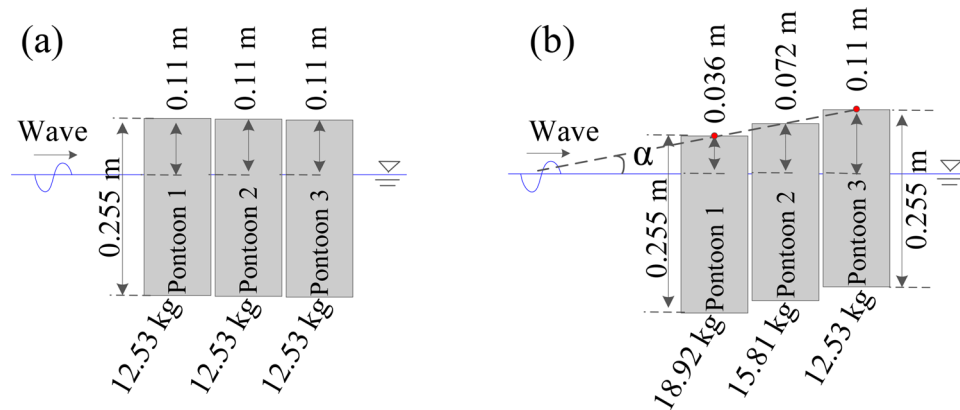


FIGURE 5 The configurations and immersion depths, and weights of three pontoons in still water, $\tan(\alpha)$ is the draft gradient between pontoon 1 and 3: (a) layout A and (b) layout B

2.2 | Experiment setup

The experimental tests were performed in a 32.00 m long, 0.50 m wide and 0.90 m deep wave flume at the Key Laboratory of Ministry of Education for Coastal Disaster and Protection, Hohai University, China. A piston-type unidirectional wave maker was installed at one end of the wave channel, and a wave absorber was located at the other end to reduce wave reflection. The physical model was mounted in the middle of the wave flume to ensure that the wave-structure interaction processes are not affected from the reflected waves from the wave maker or wave absorber. The overall experiment setup is described in Figure 4. The relative positions of wave gauges and lasers are also illustrated in the figure, whereas the distances among them are not scaled.

The floating pontoons were made of wood and filled with foam material and metal blocks. The draft was adjusted by extra ballasts; the pontoon with a larger mass has a deeper draft. The hydrodynamic characteristics of the model also changed signif-

icantly with the draft. During the experiments, two types of floating pontoon layouts were tested (1) layout A-pontoons had equal drafts and (2) layout B-pontoons had step change drafts, as shown in Figure 5. For the layout B, the gradient of draft, $\tan(\alpha)$, had the initial value of 0.185. In addition, to avoid unnecessary friction and possible collisions between pontoons and flume wall, a 1 cm clearance was used between the floating pontoons and the flume wall. There was little effect of this clearance on experimental results within the few wave periods duration of our experiments.

The experiments were conducted at a still water depth b of 0.60 m, for regular waves with a wave period T from 0.73 to 3.00 s and a wave height H from 0.017 m to 0.229 m. The selected wave period range corresponds to full-scale wave periods from 2.31 to 9.48 s, which is the dominant wave period range observed in the ocean near China [33]. The loads connected to the dynamos for pontoon 1 and pontoon 2 (see Figure 4) were 3.30 and 23.50 Ω , respectively. As summarized in Table 1, 66 test cases were conducted for wave conditions

TABLE 1 Parameters of experiments series for pontoon layouts A and B with the same and step change drafts respectively

Water depth h (m)	Wave steepness H/L	Wave period T (s)	Dynamo	Dynamo	Type of layout
			load $R_{\text{pontoon 1}}$ (Ω)	load $R_{\text{pontoon 2}}$ (Ω)	
0.60	0.02	0.73–1.80*	3.30	23.50	A; B
		2.06			
		2.41			
		3.00			
0.60	0.03	0.73–1.80*	3.30	23.50	A; B
		2.06			
		2.41			
		3.00			
0.60	0.06	0.73–1.80*	3.30	23.50	A; B

*Note: 0.73–1.80 stands for 0.73, 0.82, 0.93, 1.05, 1.20, 1.28, 1.44, 1.60 and 1.80.

under which the integrated system is expected to be efficient and economically competitive in the ocean. During each test, the free surface elevation was measured by 5 capacitance-type wave gauges, G1-G5, before and after the floating pontoons. The measurements from the three wave gauges, G2-G4, in front of the pontoons were used to separate the incident waves from the reflected waves and calculate the reflection coefficient. The gauge G5 after the pontoons provided the measurement of the transmitted wave which gives the transmission coefficient.

At the same time, the motion response of the pontoons was tracked by the three laser sensors above the pontoons. The real-time output power of the dynamos was collected by a data acquisition box. Time series at a sampling frequency of 1.00 kHz of wave and electric power output were used for the analysis in the next section. In addition to the laser system and wave gauge measurements, a video camera was used to record the interaction processes between wave and structure. Each test case listed in the table was repeated three times. During each test, all the measurements were repeated over 6 to 11 wave cycles before the arrival of the reflected waves bounced off from the wave maker. After each time step of data sampling, the relative positions of pulleys, toothed racks, gears, shafts and pontoons were checked to ensure that the joints were positioned properly.

2.3 | Data analysis

Based on the time series of wave measured by gauges G2, G3 and G4, the least squares method [34] was used to separate the incident wave height H and reflection wave height H_r . Then, the reflection coefficient K_r , defined as H_r/H , was calculated. For the transmission coefficient K_t , first, the time series of surface profile of gauge G5 is decomposed into a series of various wave frequency components using the fast Fourier transform (FFT) algorithm. Next, the energy of all these wave

components was summed up as E_t , and then K_t was calculated as

$$K_t = \sqrt{E_t/E_i} \quad (1)$$

where $E_i = 0.125\rho g H^2$ was the incident wave energy, ρ is the water density (1000 kg/m³), $g = 9.81$ m/s² is the gravitational acceleration, H is the incident wave height.

The energy loss due to wave-structure interactions was given by

$$K_{\text{loss}} = 1 - K_t^2 - K_r^2 \quad (2)$$

Note that K_{loss} includes not only the energy loss caused by viscous effects, such as vortex generation and shedding at the edge of floating pontoons and strong wave deformations and breaking, but also the energy absorbed by the PTO modules.

The incident wave power P_{wave} for a given pontoon width was estimated as follows:

$$P_{\text{wave}} = \frac{1}{16} \rho g H^2 B_b \frac{L}{T} \left[1 + \frac{\frac{4\pi b}{L}}{\sin b(\frac{4\pi b}{L})} \right] \quad (3)$$

where T is the wave period, B_b is the width of the pontoon (0.48 m), L is the wavelength and b is the still water depth.

For each pontoon equipped with a PTO module, the average output power P_{average} was estimated by summing the energy consumed by the dissipative force T_d and the instantaneous power generated by the dynamo with respect to one wave period.

$$P_{\text{average}} = \frac{1}{T} \int_t^{t+T} P_{\text{pontoon}} dt = \frac{1}{T} \int_t^{t+T} \left(\frac{U_{\text{dynamo}}^2}{R_{\text{pontoon}}} + T_d \times \Delta z \right) dt \quad (4)$$

where P_{pontoon} is the instantaneous power generated by pontoons, T_d is the dissipative force from racks and gearboxes, Δz is the vertical displacement of the pontoon within each time step, U_{dynamo} is the real-time voltage output of dynamos, and R_{pontoon} is the dynamo load. Using the no-load measurement tests, the dissipative forces T_d acting on pontoon 1 and pontoon 2 were estimated to be around 5.98 and 5.39 N, respectively.

For the integrated device, the total average output power P_{out} was calculated as

$$P_{\text{out}} = P_{\text{average_pontoon1}} + P_{\text{average_pontoon2}} \quad (5)$$

where $P_{\text{average_pontoon1}}$ and $P_{\text{average_pontoon2}}$ are the average output power of pontoon 1 and pontoon 2, respectively.

Finally, the hydrodynamic efficiency K_{hydro} for wave energy extraction $K_{\text{hydro}} = P_{\text{out}}/P_{\text{wave}}$ were calculated to assess the performance of WECs.

Layout A

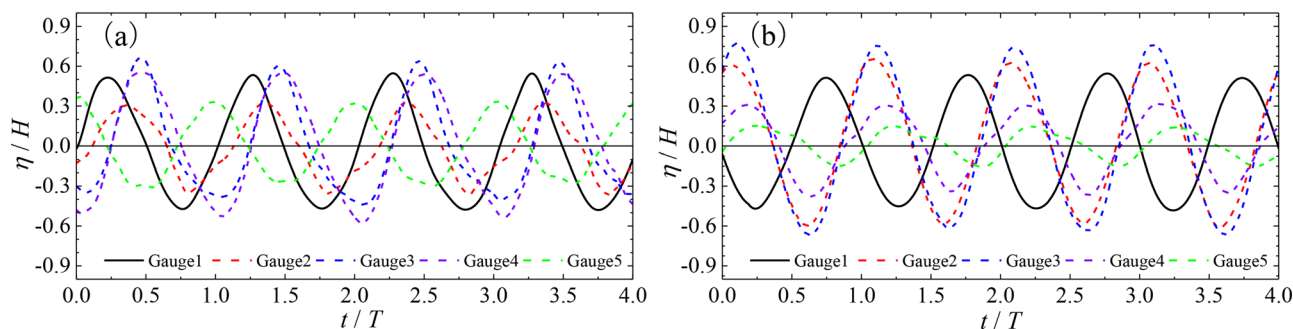


FIGURE 6 The measured surface elevations by Gauge 1 (black solid line), Gauge 2 (red dashed line), Gauge 3 (blue dashed line), Gauge 4 (violet dashed line), and Gauge 5 (green dashed line) before and after the integrated system for layout A: (a) $T = 1.80$ s, $b = 0.60$ m, $H/L = 0.03$, $L = 3.82$ m and (b) $T = 1.05$ s, $b = 0.60$ m, $H/L = 0.03$, $L = 1.68$ m

Layout B

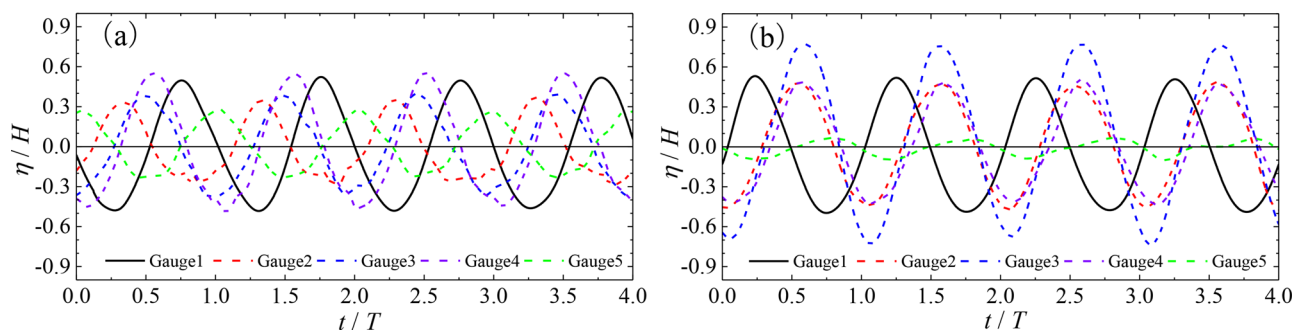


FIGURE 7 Measured surface elevations by Gauge 1 (black solid line), Gauge 2 (red dashed line), Gauge 3 (blue dashed line), Gauge 4 (violet dashed line), and Gauge 5 (green dashed line) before and after the integrated system for layout B: (a) $T = 1.80$ s, $b = 0.60$ m, $H/L = 0.03$, $L = 3.82$ m; and (b) $T = 1.05$ s, $b = 0.60$ m, $H/L = 0.03$, $L = 1.68$ m

3 | RESULTS AND DISCUSSION

3.1 | Water surface elevations

As previously mentioned, various wave steepness H/L were employed in the experimental tests for both layout A and B. When H/L is equal to 0.03, the incident wave is weakly non-linear so that significant deformation of the water shape occurs after the wave passed the hybrid system. Figures 6 and 7 present the time series of free surface elevations for layout A and B. Each of these two figures shows two test cases with the same wave steepness but two different wave period of $T = 1.80$ s (Figures 6(a) and 7(a)) and $T = 1.05$ s (Figures 6(b) and 7(b)).

For the longer wave of $T = 1.80$ s, as shown in Figures 6(a) and 7(a), the non-linearity of the superposed wave can be recognized on the weather side of the buoys, and the wave is transmitted moderately across the pontoons to the leeward side. When the pontoons are arranged as layout A, wave overtopping is less likely to occur as the top surface of the front pontoon 1 is high; therefore, a standing wave may form in front of the pontoons for both wave periods. According to the theory of standing waves, the wave amplitude is attenuated at gauges close to

the nodes, such as gauge 2 in Figure 6(a) and gauge 4 in Figure 6(b), while at gauges near the antinodes, the wave amplitude is enlarged, such as that at gauge 3 in Figure 6(a,b). Meanwhile, it can be observed that after interaction with the structure, the transmitted wave is distributed over a wider frequency band, and higher harmonics are generated accompanied by the primary wave component. Furthermore, comparison of the data of gauge 5 for $T = 1.80$ s (Figure 6(a)) and $T = 1.05$ s (Figure 6(b)) indicated that the wave height decreases more across the structure for shorter waves. This may be due to the shorter wavelength and smaller wave force at a smaller wave period, thus decrease the transmitted waves and the radiated waves produced by the pontoon motion. After energy dissipation by the floating pontoons, the wave height is only approximately 30.11% of the incident height at gauge 5, as seen in Figure 6(b). In contrast, Figure 6(a) shows that at relatively long wavelength, it is easier for the incoming wave to pass under the floating pontoons or drive the floating pontoons to radiate energy to the rear. Therefore, the transmitted wave height can reach approximately 64.17% of the original wave height even though a part of the wave energy is reflected back to the paddle and another part of the wave energy is converted by the PTO modules.

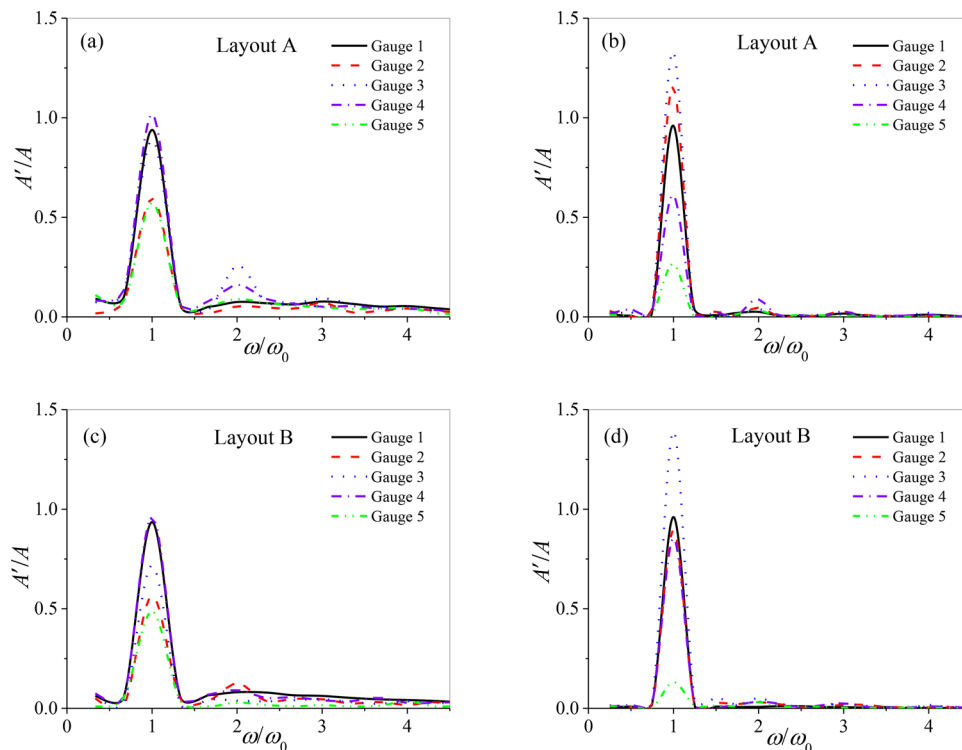


FIGURE 8 Normalized free surface elevation amplitude spectra of incident wave (Gauge 1: black solid line), wave in front of the pontoons (Gauge 2: red dashed line; Gauge 3: blue dotted line; Gauge 4: violet dashed-dotted line) and transmitted wave after the pontoons (Gauge 5: green dashed-dotted-dotted line): (a) and (c) $T = 1.80$ s, $b = 0.60$ m, $H/L = 0.03$, $L = 3.82$ m; (b) and (d) $T = 1.05$ s, $b = 0.60$ m, $H/L = 0.03$, $L = 1.68$ m (see gauges locations indicated by Figure 4)

When the three floating pontoons have different immersion depths (i.e. layout B) and their top surfaces form a stepped plane, the interaction process between the pontoons and water waves becomes more complex. In addition to standing waves due to wave reflection, the interaction process is also affected by potential wave overtopping and breaking in case of large waves [35]. More energy transfers from the lower order to higher orders, along with viscous dissipation and energy loss due to strong wave deformations [28, 29]. Consequently, the wave heights behind the stepped pontoons shown in Figure 7(a,b) are 20.25% and 49.64% lower than those for layout A for wave period $T = 1.8$ s and 1.05 s respectively, implying more wave attenuation for the layout B. In addition, we conducted spectral analysis of the free water surface elevations at gauges 1–5 for the same cases in Figures 6 and 7. The variation of normalized wave amplitude for different tests is plotted in Figure 8. Note that ω is the angular frequency, A' is the amplitude of wave components, ω_0 and A are the angular frequency and the wave amplitude of incident wave at the peak frequency, respectively. As shown in the figure, the primary and second-order wave components for incident waves (gauge 1) are similar for all these four cases as the wave steepness is the same. After the wave encounters with the pontoons, the surface elevation spectra change dramatically, especially for layout A in a longer wave ($T = 1.80$ s). As shown in Figure 8(a), the second-order harmonic component of the wave surface is significant at gauges 3 and 4. This may be explained by the non-linearity embedded in the wave-structure interac-

tion which causes the wave energy to be transferred from the first-order primary wave to the second-order harmonic wave. However, due to the weak transmission at the second-order harmonic frequency, the wave amplitude of the second-order component is limited behind the pontoons (gauge 5). For $T = 1.05$ s, a large proportion of incident wave energy is reflected back to the weather side, leading to an enlargement of wave amplitude in front of the pontoons. In contrast, the normalized wave amplitude at the leeside of the hybrid system is small due to the wave reflection, which is consistent with the finding in Figure 6. The energy transfer from the primary wave to the harmonic waves is less evident for layout B than that for layout A. This feature may be explained by the fact that a considerable part of wave energy is consumed by the generation of eddies and the wave breaking induced by the top surfaces of pontoons.

The free surface elevation and flow field above floating pontoons would help to understand the mechanisms for the wave deformation. The snapshots of the interaction between the waves and floating pontoons are shown in Figures 9 and 10 for layout A and layout B, respectively, with $T = 1.80$ s, $b = 0.60$ m, and $H/L = 0.06$. In Figure 9(a), non-linear wave deformations, such as wave overtopping and breaking, are observed, as the wave crest is higher than the elevation of the top surface of pontoon 1. At this time, the draft gradient $\tan(\alpha)$ is negative (-0.145) because pontoon 3 is lower than pontoon 1, and the downward slope, is shown to block the incoming wave to some extent. After a quarter of the wave period, at $t = 34.24$ s, the rear

Layout A

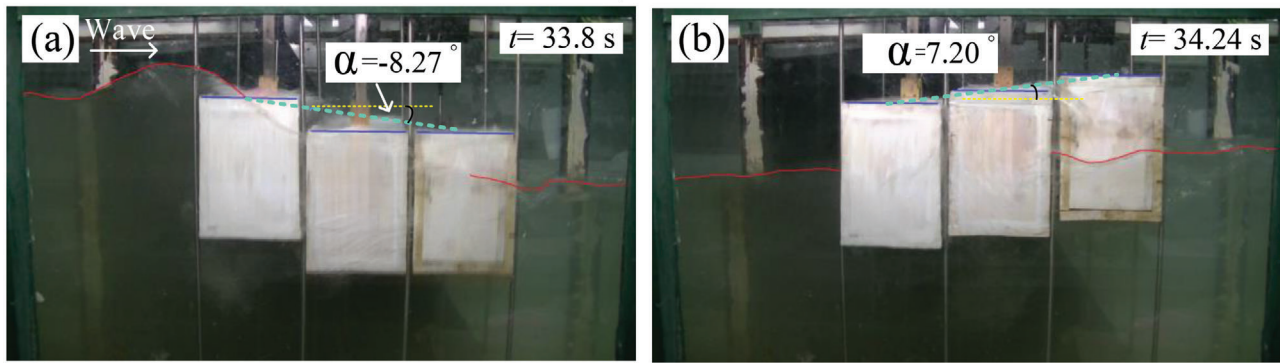


FIGURE 9 Snapshots of the wave-structure interaction for layout A for wave conditions $T = 1.80$ s, $b = 0.60$ m, $H/L = 0.06$: at time instant (a) $t = 33.8$ s and (b) $t = 34.24$ s. Dashed line in cyan colour is the slope formed by pontoons 1 and 3, the red solid line indicates water surface, the dashed yellow line is the horizontal line

Layout B

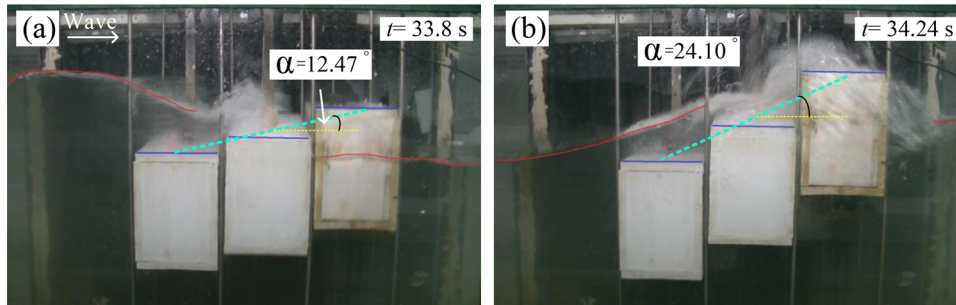


FIGURE 10 Snapshots of the wave-structure interaction for layout B in the case of $T = 1.80$ s, $b = 0.60$ m, $H/L = 0.06$: (a) $t = 33.8$ s and (b) $t = 34.24$ s. Dash line in cyan colour is the slope formed by pontoons, the red solid line indicates water surface, the dashed yellow line is horizontal line

two pontoons rise to higher elevations leading to positive the draft gradient of $\tan(\alpha) = 0.126$ at the instant. The kinematic characteristics of the pontoons is different for layout B from that for layout A. It was observed that the draft gradient of the slope formulated by the upper planes of the pontoons in layout B remains positive during the experiments. The non-linearity embedded in Figure 10 as indicated by considerable mixing air-fluid is more noticeable than that in Figure 9, indicating a more complicated wave-structure interaction. In Figure 10(a), the external forces from overtopping water and wave breaking considerably suppressed the upward movements of pontoons, especially pontoon 1, with strong vortices formed near the corners of the front pontoons. Subsequently, in Figure 10(b), the draft gradient $\tan(\alpha)$ indicated by the straight dashed line in cyan colour reaches approximately 0.447 ($\alpha = 24.10^\circ$), which is more than twice as the initial value $\tan(\alpha) = 0.185$. In the meantime, the surfaces of pontoons 2 and 3 encountered violent wave slamming due to wave breaking similar to that in front of a vertical breakwater or seawall, as indicated by the extensive white plume of air-water mixture, which dissipated a considerable portion of the incoming wave energy. Those slamming loads can be destructive under extreme conditions and thereby are of great importance for device survivability, as suggested by

other researchers [36, 37]. In the next section, the authors will investigate the effect of slamming on the performance and survivability of the integrated system using numerical modelling.

3.2 | Wave reflection and transmission coefficient and energy loss rate

The reflection coefficient K_r , transmission coefficient K_t , energy loss rate K_{loss} and energy dissipation $K_{\text{loss}} - K_{\text{hydro}}$ due to the viscous effect, friction loss etc. are plotted in Figure 11 as a function of the non-dimensional wavelength for layouts A and B, respectively. Note that k is the wave number and is defined as $k = 2\pi/L$. In the figure, the effects of wave steepness and wave period on wave reflection, transmission and dissipation are emphasized. The wave transformation characteristics and the wave non-linearity indicated by wave steepness play an important role in the wave attenuation of the hybrid WEC-breakwater system [38]. The variation of wave reflection coefficient, transmission coefficient and energy loss rate help to evaluate the separate contribution of wave energy extraction to the overall capacity to alleviate the storm damage to the coast behind the system.

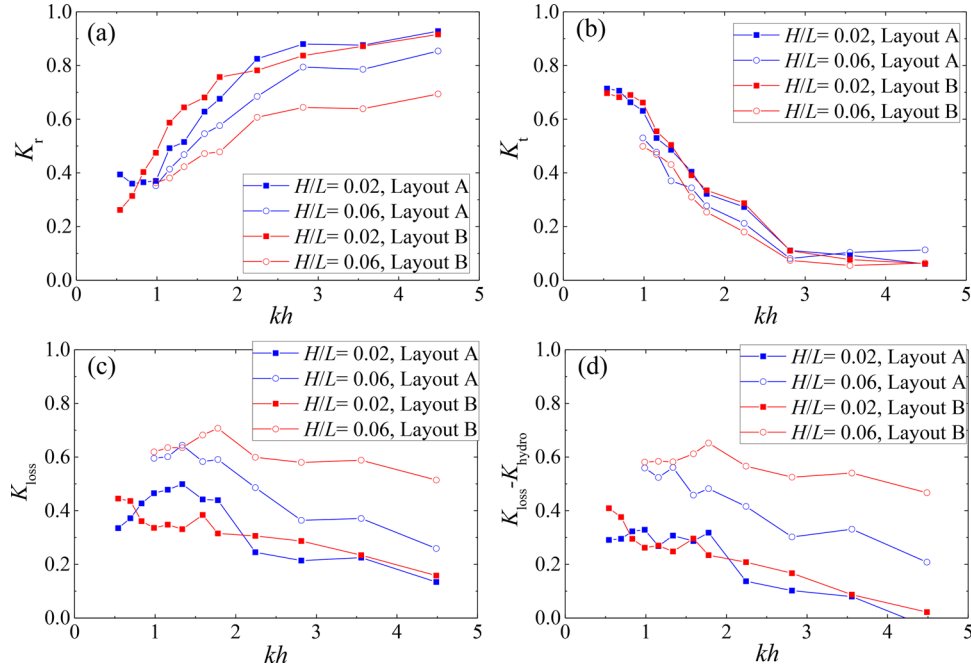


FIGURE 11 The (a) reflection coefficient K_r , (b) transmission coefficient K_t , (c) energy loss rate K_{loss} and (d) energy dissipation $K_{loss} - K_{hydro}$ for layouts A and B vs kh for wave steepness $H/L = 0.02$ (blue and red squares) and 0.06 (blue and red circles)

For all experiments, the PTO damping and water depth are kept constant. Figure 11(a) indicates that K_r increases with increasing frequency, except for the cases with the lowest values of kh for layout A. At high wave frequencies, the displacement of the floating pontoons are small as the heave exciting force is weak, as discussed by Drimer et al. [39]. As a result, pontoon 1 in the front, acts like a fixed vertical structure that reflects the incoming wave effectively, so that K_r is close to 1.00. The external excitation force increases with decreasing frequency so that the displacement of the floating pontoons increases with increasing wave period under the action of intermediate and long waves. As mentioned in Section 3.1, significant portion of incident wave energy at low frequencies may be transmitted across the pontoons causing K_t to decrease rapidly to about 0.35. For layout type B, the reflection coefficient is smaller than that of layout A for the larger waves (with a large period or high wave steepness). Comparison of K_r for both layouts indicates that the wave reflection at low frequencies is reduced by approximately 29.59% by the pontoon configuration change from layout A to layout B with different drafts among pontoons.

Furthermore, for layout B, a larger wave steepness may have adverse effects on the performance of the present device in reflecting waves, which is more evident at high frequencies (K_r decreases by 25.33% at $kh = 4.49$) than low frequencies (K_r decreases by 18.97% at $kh = 0.99$). This is mainly due to the fact the non-linearity of higher frequency waves makes the waves more easily break and dissipate the energy. In contrast to K_r , the transmission coefficient K_t decreases with increasing non-dimensional wavelength. Figure 11(b) shows that transmission coefficient K_t for pontoons with varying draft in layout B is slightly lower than that of pontoons with equal draft in layout

A. At low frequencies, the averaged K_t is 0.65 in both layouts A and B, implying that the transmitted wave height is less than half of the incident wave height, and that the present system is capable to effectively suppress the wave transmission.

Given K_r and K_t , the energy loss rate K_{loss} can be calculated using Equation (2). K_{loss} consists of the contribution from both the viscous dissipation during the fluid-structure interaction process and the wave energy converted electric energy by the PTO modules. After subtracting the hydrodynamic efficiency K_{hydro} , the energy loss by viscous dissipation can be obtained, as shown in Figure 11(d). Figure 11(c) shows that unlike K_r and K_t , K_{loss} first increases and then decreases as the frequency increases. This is mainly due to the high energy conversion efficiency of the developed device in moderate waves, which consumes a considerable portion of the wave power. As shown in Figure 11(d), the subtraction of K_{hydro} from K_{loss} fairly modifies the variation tendency of the energy dissipation rate as a function of the dimensionless wavelength. The energy dissipation caused by viscous effects decreases with increasing wave frequency. The energy loss rate increases when the integrated system operates under waves with greater heights. This increase in K_{loss} is also related to the viscous losses during wave-structure interactions which is more significant for layout B. For medium and longer waves ($kh < 2.24$), the average K_{loss} is approximately 0.48, with nearly half of the incident wave energy being dissipated. More notably, when the incident wave height is large (the wave steepness is 0.06 or the wave period is greater than 1.80 s), the energy loss at layout B is much larger than that at layout A. In the case of strong non-linearity ($H/L = 0.06$), the average K_{loss} is estimated to be 0.62. Differing from the situation of layout A, the energy loss for layout B mainly comes from viscous

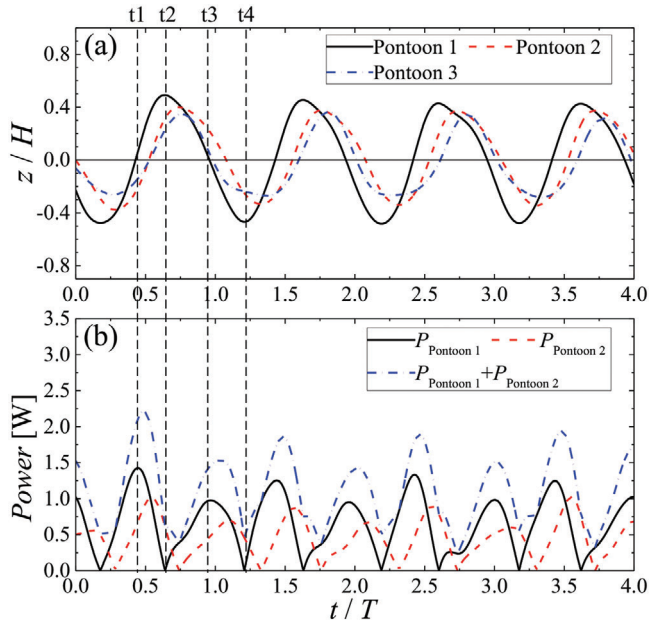


FIGURE 12 (a) Vertical displacement normalized by wave height and (b) output power of pontoon 1 (black solid line), pontoon 2 (red dashed line) and the sum (blue dashed-dotted line) for layout A at $T=1.80$ s, $b=0.60$ m, and $H/L=0.03$

dissipation, and the contribution of wave energy conversion to electric power is not apparent, which will be discussed further in the following sections.

3.3 | Dynamic response of floating pontoons

For the present integrated system, the wave energy is harnessed from the vertical motion of floating pontoons, therefore, the dynamic response of the pontoons to wave forcing is critical to the performance of the system. The normalized vertical displacement of the pontoons relative to the wave height z/H and output power of pontoon 1 and pontoon 2 are plotted against the dimensionless time for four wave cycles in Figure 12 for layout A and wave condition $T=1.08$ s, $H/L=0.03$ and $b=0.6$ m. The four dashed lines mark different time instants, namely, t_1 – t_4 , to highlight the results. The initial elevations of pontoons have been deducted to obtain the vertical displacement in Figure 12. The positive and negative vertical displacement z/H indicates the pontoons moved upwards and downwards from its initial position respectively. The pontoon displacement oscillates with time since the external excitation force from the wave is periodic. Pontoon 1 is the first to respond when the wave approaches the hybrid device; therefore, the motion is out of phase by approximately $\pi/4$ with the others, as evident in Figure 12(a). Furthermore, the response amplitudes of pontoons can be estimated based on the data recorded in the experiments. Although pontoon 1 is damped by the PTO module, its motion amplitude is much larger than those of the other two, so that the energy output by Pontoon 1 dominates the total energy conversion. As shown in Figure 12(b), the instanta-

neous power also oscillates with the time, and the peak total power (blue dashed-dotted line) is approximately 2.21 W. At t_2 and t_4 , the pontoon 1 attains the maximum and minimum vertical displacement z/H and therefore, the minimum vertical velocity magnitude. It follows the output power in Figure 12(b) dropped to nearly zero at t_2 and t_4 , i.e. twice within one wave cycle, which is different from the vertical displacement of the pontoons in Figure 12(a). In contrast, the velocity of pontoons approach peak values as the pontoons return to an equilibrium position at t_1 and t_3 leading to two peak output power at t_1 and t_3 . Note that the phase lag between the output power of pontoon 1 and pontoon 2 is critical in smoothing out power fluctuations [40].

This can be confirmed by comparing the normalized standard deviation (NSD) for the time series of instantaneous output power. NSD can be calculated using Equation (6).

$$NSD = \frac{\sqrt{\frac{1}{N} \sum_{i=1}^N (X_i - \bar{X})^2}}{\bar{X}} \quad (6)$$

where X_i is the value of the i th sample in the data set, \bar{X} is the mean value of the data set, and N is the number of samples in the data set.

The estimated NSDs of the output power are summarized in Table 2 for pontoon layout A and B. Table 2 indicates that the deviation of the total output power is smaller than that of pontoon 1 or pontoon 2, and the instability of wave power conversion can be reduced by using the integrated WEC-floating breakwater with multiple pontoons. According to Table 2, the averaged NSDs for individual pontoons are decreases by 22.81% and 23.65% at layouts A and B, respectively, after being integrated with each other as one WEC. This finding is likely applicable to irregular waves. Moreover, the instability of the wave conversion may be further improved if more pontoons are used and/or a well-designed control strategy is applied. Finally, the average output power of the WEC-breakwater system may be calculated from the data in Figure 12(b) using Equation (4) in the next section.

The vertical displacement amplitude normalized by the wave height $(z_{\max} - z_{\min})/2A$ of the floating pontoons are shown in Figure 13 as a function of the relative depth kb for layouts A and B. The kinematical characteristics of these floating pontoons differ from each other due to the difference in their locations, drafts and loads. The pontoon 3, in particular, responds in a pattern distinct from that of pontoon 1 and pontoon 2, especially to short and intermediate waves. Under shorter waves ($kb > 2.24$), Pontoon 3 oscillates vertically with a larger amplitude than pontoons 1 and 2 in front of it because its heave motion is not damped by PTO like pontoons 1 and 2, although pontoon 3 is farthest from the incoming wave. In contrast, the first two pontoons tend to maintain their positions, as the wave force is too small to overcome the damping force from the PTO modules. However, as the wave period increases (i.e. kb decreases), the dimensionless responses of pontoons 1 and 2 increase rapidly, and eventually, their amplitudes exceed that of pontoon 3 in intermediate waves. In contrast, the displacement of pontoon 3

TABLE 2 Normalized standard deviation (NSD) for the time series of instantaneous output power for water depth $b = 0.6$ m and wave steepness $H/L = 0.03$

T (s)	Layout A			Layout B		
	$P_{\text{pontoon 1}}$	$P_{\text{pontoon 2}}$	$P_{\text{pontoon 1}} + P_{\text{pontoon 2}}$	$P_{\text{pontoon 1}}$	$P_{\text{pontoon 2}}$	$P_{\text{pontoon 1}} + P_{\text{pontoon 2}}$
Averaged NSD for various T	0.492	0.503	0.387	0.555	0.540	0.418

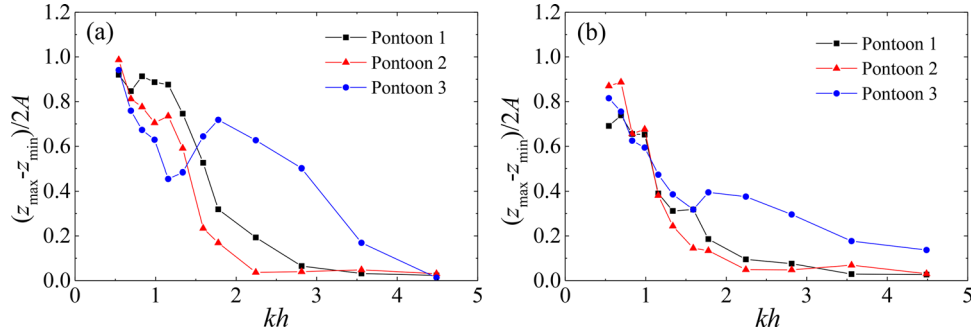


FIGURE 13 Normalized vertical displacement amplitudes of pontoon 1 (black square), pontoon 2 (red triangle) and pontoon 3 (blue circle) for water depth $b = 0.60$ m and wave steepness $H/L = 0.03$: (a) layout A and (b) layout B

drops to minimum in the mid-range of wave frequencies due to the wave attenuation by the front two pontoons. As the period of the incoming wave increases, the normalized displacement for pontoons 1–3 can reach up to approximately 1.00 for layout A in response to the longest waves. These pontoons have sufficient time to accelerate or decelerate and thereby remain synchronized with the wave surface motion with long wave period. As a result, most of the incident wave energy is transmitted to the leeward side of the WEC for longer waves as shown in Figures 6 and 11. In contrast, for layout B, the wave overtopping at the top of pontoons at large wave heights suppressed the pontoon motions significantly, as seen in Figure 13(b); accordingly, the response amplitude decreases dramatically, especially for pontoon 1.

As mentioned in Section 3.1, the draft gradient $\tan(\alpha)$ (see Figures 5, 9, and 10) is useful for determining the energy loss caused by viscosity. Meanwhile, it should be noted that the amplitude of this gradient cannot be computed using the data in Figure 13, owing to the phase lag among pontoon motions. Figure 14 presents the maximum and minimum values of the draft gradient that are estimated directly using the time history of pontoon displacements. For layout A, $\tan(\alpha)$ oscillates between positive and negative values within one wave period, while the magnitude of the negative minimum is slightly larger than that of the positive maximum in most cases. This leads to a large displacement of pontoons, therefore large wave energy conversion but unfavourable enhanced viscous losses. For layout B, the initial gradient is 0.185, which is also included in the figure. Differing from layout A, $\tan(\alpha)$ is always positive during the experiment for layout B. At low and intermediate frequencies, $\tan(\alpha)$ is enlarged as a result of the aforementioned damping force associated with wave overtopping and breaking waves. The gradient can reach up to 0.38 under the action of

the longest wave, which is conducive to large wave attenuation, especially for large waves.

3.4 | Wave energy conversion

In this section, the time average output power of pontoons 1 and 2 are added to obtain the overall power output P_{out} , calculated with Equations (4) and (5) using the data in Figure 12(b). The hydrodynamic efficiency K_{hydro} for wave energy conversion is given by $K_{\text{hydro}} = P_{\text{out}}/P_{\text{wave}}$ and illustrated in Figure 15(b).

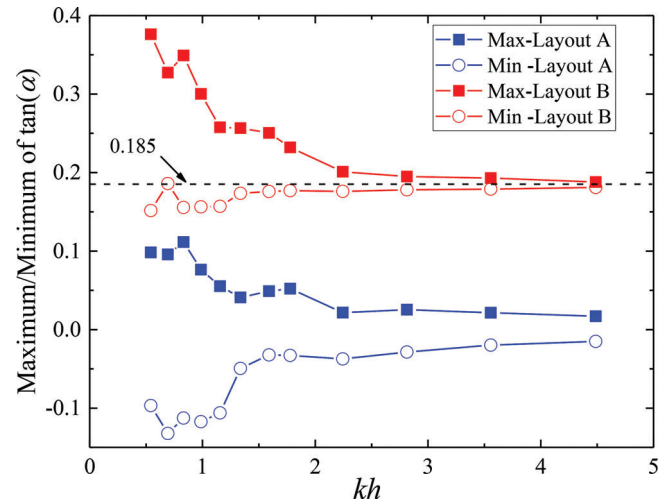


FIGURE 14 Maximum (blue and red squares) and minimum (blue and red circles) draft gradient $\tan(\alpha)$ of pontoons for water depth $b = 0.60$ m, and steepness $H/L = 0.03$ and for layout A and B

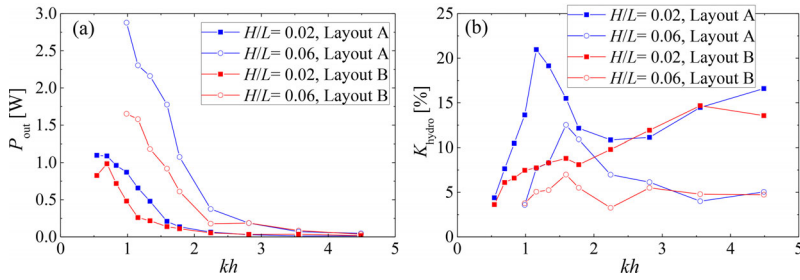


FIGURE 15 (a) Time average output power and (b) hydrodynamic efficiency of the hybrid system of layouts A (blue square and blue circle) and B (red square and red circle) vs kh for different wave steepness H/L .

The experimental results of P_{out} as a function of the relative water depth (kh) are shown in Figure 15(a), while the water depth and the PTO damping are kept constant. P_{out} is higher when the incoming wave power is high (with a large period or high wave steepness). The highest average output power is approximately 2.88 W, with a wave period T of 1.80 s and a wave steepness H/L of 0.06. Similar to the output power results, the hydrodynamic efficiency in the figure are also calculated using the sum of the wave power produced by pontoons 1 and 2. The effects of the wave period and wave steepness on K_{hydro} are highlighted by Figure 15(b). For shorter waves ($kh > 2.24$) at a lower wave steepness (0.02 or 0.03), the hydrodynamic efficiency of the system is acceptable, but the average power output is very small in these cases, possibly due to the fact that the short waves are not high enough to cause significant energy loss associated with wave breaking or other dissipating processes. When $kh < 2.24$, results for layout A in Figure 15(b) show that the ratio of the captured energy to the incident energy increases with decreasing relative depth kh to a maximum and then decreases with decreasing kh , showing a parabolic curve since a larger wave force is beneficial to energy conversion but the complex flow induced by low frequency waves hinders wave power extraction abilities [41]. Noted that although the output power is higher at higher incoming wave energy the energy conversion efficiency is lower. When the device is deployed in a less energetic sea state, the efficiency is higher, but the output power is lower. Then, the maximum energy conversion efficiency (20.97%) is achieved at medium frequencies with a wave steepness of 0.02. This may be attributed to the energy loss caused by viscosity associated with a relatively larger wave force of high sea state and a stronger non-linearity of the longer waves [38]. Consequently, the proposed WEC-floating breakwater hybrid system has a higher efficiency under low sea states and a lower efficiency under high sea state, therefore reducing the instability of the electricity grid caused by the variability of wave power output of high and low sea states. Contrary to our expectations, increasing wave height decrease the energy conversion efficiency at most wave frequencies. This finding is consistent with that by Wang et al. [42] who proposed that the efficiency decreases with the wave amplitude due to the combined effect of the non-linearity and viscosity. The non-linearity of wave interactions with floating pontoons is closely related to the wave steepness [43]. For a fixed wave period, the velocity of water particles is proportional to the wave steepness. Larger wave steepness, therefore, leads to larger dissipation caused by vortex shedding at the edge

of the floating pontoons. The vortex shedding induced dissipation at OWC was also observed by Zhang et al. [44] from their two phase flow modelling. In addition, Figure 13(a) shows that the displacement of pontoons is amplified by large waves, which in turn reduce the effectiveness of the device in capturing wave energy, especially for lower frequency large waves. This behaviour may help to protect the device during extreme storms [45].

As shown in Figure 15(a), the variation trend of P_{out} for layout B is similar to that of layout A but with smaller values in general, except for the longest waves. For $kh > 2.24$, the hydrodynamic efficiency for layout B is comparable to that of layout A. However, as the wave period increases, the turbulence and vortex shedding are intensified leading to stronger dissipation, therefore lower device efficiency and less wave reflection. As shown in Figures 9 and 10, under longer waves, wave overtopping and strong non-linear deformations of the water surface above the pontoons increase the wave attenuation and decrease the energy extraction. It was observed in wave tank experiment that wave overtopping also caused complex turbulent fields and flow patterns around wave energy buoys-breakwater, thereby increased the energy loss in the experiments [12]. Therefore, the proposed hybrid device at layout B is more efficient as a breakwater to protect the coast, but less effective as a wave energy converter. In the next step, parametric analyses of the pontoons will be used to optimize the configuration of the present hybrid system that balances the need of both energy converter and breakwater. Moreover, a control strategy for the PTO system will also be explored for dominant wave conditions considering both cost-efficient wave energy harvest and structure integrity, as suggested by Nguyen and Tona [46].

4 | CONCLUSIONS

This paper proposed a novel hybrid wave energy conversion and floating breakwater system consisting three closely arranged floating pontoons. The hydrodynamics characterization of the system were assessed in a wave flume at a geometric scale of 1/10 to shed new light on the subject. The influence of the PTO modules on the performance of the system as a breakwater and WECs were investigated based on experimental measurements. In addition, the effect of the configuration of pontoons was also examined under various wave conditions. The major conclusions are summarized below:

1. The hybrid system with triple pontoons with step change draft (layout B) is robust in attenuating the wave energy mainly through viscous effects at medium and low wave frequencies, with an average K_{loss} close to 0.48. However, for the system of triple pontoons with same draft (layout A), the PTO modules also contribute considerably to the wave attenuation.
2. The integration of power outputs from two PTO modules is beneficial to the stability of the total power outputs to the grid. Due to the phase lag between pontoon displacements, the peak power output of individual pontoon appear at different times. As a result, the averaged normalized standard deviation (NSD) of power output is reduced by approximately 22.81% and 23.65% under layouts A and B, respectively, by combining the output of pontoons.
3. The displacement amplitude of pontoon 3 is larger under shorter waves as it is free of PTO damping, whereas that of pontoons 1 and 2 is smaller due to the resistance of the PTO modules. Under longer wave, however, the displacement of pontoons 1 and 2 exceeds that of pontoon 3, reaching about the incident wave height $2A$ under longer waves.
4. In case of layout B, the three pontoons oscillated in distinct patterns due to varied weights and immersion depths. The draft gradient $\tan(\alpha)$ is always positive and enlarged at low and intermediate frequencies due to the damping force associated with wave overtopping and breaking waves, leading to strong non-linear wave deformations and then wave energy dissipation. In case of layout A, the draft gradient $\tan(\alpha)$ alternates between negative and positive values, which is disadvantageous for wave attenuation.
5. The wave overtopping and strong non-linear deformations of the water surface above the pontoons increase the wave attenuation and decrease the energy extraction. As a result, the highest hydrodynamic efficiency of wave energy conversion (20.97%) is achieved in moderate waves ($T = 1.60$ s, $b = 0.60$ m, $H/L = 0.02$) when the system is arranged as layout A. The hybrid system in layout B is more efficient as a breakwater to protect the coast, but less effective as a wave energy converter.

ACKNOWLEDGMENTS

The research was funded by [National Natural Science Foundation of China](#) (U1706230, 51709095), the [Fundamental Research Funds for the Central Universities](#) (B210202028) and the Marine Renewable Energy Foundation, State Oceanic Administration, China (GHME2017YY01). Authors are also grateful to the reviewers of this paper for their helpful comments.

ORCID

Wei Peng  <https://orcid.org/0000-0002-5756-1381>

REFERENCES

1. Falnes, J.: A review of wave-energy extraction. *Mar. Struct.* 20(4), 185–201 (2007)
2. Zhang, Y., Lin, Z., Liu, Q.: Marine renewable energy in China: Current status and perspectives. *Water Sci. Eng.* 7(3), 288–305 (2014)
3. Alcorn, R., Beattie, W.: Observations of time domain data on the wells turbine in the islay wave-power plant. In: *Proceedings of the 8th International Offshore and Polar Engineering Conference (ISOPE)*. Montreal, Canada (1998)
4. Vicinanza, D., Frigaard, P.: Wave pressure acting on a seawave slot-cone generator. *Coastal Eng.* 55(6), 553–568 (2008)
5. Li, G., et al.: Wave energy converter control by wave prediction and dynamic programming. *Renewable Energy* 48, 392–403 (2012)
6. Lucas, J., et al.: Development of a wave energy converter (WEC) design tool - application to the waveroller WEC including validation of numerical estimates. In: *Proceedings of the 4th International Conference on Ocean Energy (ICOE)*. Dublin, Ireland (2012)
7. Stratigaki, V., et al.: Wave basin experiments with large wave energy converter arrays to study interactions between the converters and effects on other users in the sea and the coastal area. *Energies* 7(2), 701–734 (2014)
8. Chow, Y.C., et al.: Experimental investigations on wave energy capture of two bottom-hinged-flap WECs operating in tandem. *Ocean Eng.* 164, 322–331 (2018)
9. Yang, S., et al.: Experimental study on the performance of a floating array-point-raft wave energy converter under random wave conditions. *Renewable Energy* 139, 538–550 (2019)
10. Martinelli, L., et al.: Hydraulic experiments on a small-scale wave energy converter with an unconventional dummy PTO. *Energies* 12(7), 1218 (2019)
11. Lopez, I., et al.: Review of wave energy technologies and the necessary power-equipment. *Renewable Sustainable Energy Rev.* 27, 413–434 (2013)
12. Reabroy, R., et al.: Hydrodynamic response and power efficiency analysis of heaving wave energy converter integrated with breakwater. *Energy Convers. Manage.* 195, 1174–1186 (2019)
13. Cascajo, R., et al.: Integration of marine wave energy converters into seaports: A case study in the port of valencia. *Energies* 12(5), 787 (2019)
14. Mustapa, M.A., et al.: Wave energy device and breakwater integration: A review. *Renewable Sustainable Energy Rev.* 77, 43–58 (2017)
15. Zhao, X.L., et al.: Hybrid floating breakwater-WEC system: A review. *Ocean Eng.* 186, 106126 (2019)
16. Perez-Collazo, C., Greaves, D., Iglesias, G.: A review of combined wave and offshore wind energy. *Renewable Sustainable Energy Rev.* 42, 141–153 (2015)
17. Muliawan, M.J., et al.: Stc (spar-torus combination): A combined spar-type floating wind turbine and large point absorber floating wave energy converter—promising and challenging. In: *Proceedings of the 31st International Conference on Ocean, Offshore and Arctic Engineering (OMAE)*. Rio de Janeiro, Brazil (2012)
18. Nguyen, H.P., Wang, C.M.: Heaving wave energy converter -type attachments to a pontoon-type very large floating structure. *Eng. Struct.* 219, 110964 (2020)
19. Palma, G., et al.: Numerical simulations of the hydraulic performance of a breakwater-integrated overtopping wave energy converter. *J. Mar. Sci. Eng.* 7(2), 38 (2019)
20. Ashlin, S.J., Sannasiraj, S.A., Sundar, V.: Performance of an array of oscillating water column devices integrated with an offshore detached breakwater. *Ocean Eng.* 163, 518–532 (2018)
21. Peng, W., et al.: Numerical analysis and performance optimization of a submerged wave energy converting device based on the floating breakwater. *J. Renewable Sustainable Energy* 9, 044503 (2017)
22. Vicinanza, D., et al.: Review of innovative harbor breakwaters for wave-energy conversion. *J. Waterw. Port Coastal Ocean Eng.* 145(4), 03119001 (2019)
23. Peng, W., et al.: Study on hydrodynamic efficiency of a multi-float wave energy converting device. In: *Proceedings of the 14th ISOPE Pacific Asia Offshore Mechanics Symposium (PACOMS)*. Dalian, China (2020)
24. Koo, W.: Nonlinear time-domain analysis of motion-restrained pneumatic floating breakwater. *Ocean Eng.* 36(9-10), 723–731 (2009)

25. He, F., Leng, J., Zhao, X.: An experimental investigation into the wave power extraction of a floating box-type breakwater with dual pneumatic chambers. *Appl. Ocean Res.* 67, 21–30 (2017)
26. He, F., Huang, Z., Law, A.W.-K.: An experimental study of a floating breakwater with asymmetric pneumatic chambers for wave energy extraction. *Appl. Energy* 106, 222–231 (2013)
27. Martinelli, L., Ruol, P., Favaretto, C.: Hybrid structure combining a wave energy converter and a floating breakwater. In: *Proceedings of the 26th International Ocean and Polar Engineering Conference (ISOPE)*. Rhodes, Greece (2016)
28. Ning, D., et al.: Hydrodynamic performance of a pile-restrained WEC-type floating breakwater: An experimental study. *Renewable Energy* 95, 531–541 (2016)
29. Ning, D.-Z., et al.: Analytical investigation of hydrodynamic performance of a dual pontoon WEC-type breakwater. *Appl. Ocean Res.* 65, 102–111 (2017)
30. Ning, D., et al.: Hydrodynamic performance of an array of wave energy converters integrated with a pontoon-type breakwater. *Energies* 11(3), 685 (2018)
31. Zhao, X., Ning, D.: Experimental investigation of breakwater-type WEC composed of both stationary and floating pontoons. *Energy* 155, 226–233 (2018)
32. Guo, B., et al.: Hydrodynamic performance of a novel WEC-breakwater integrated system consisting of triple dual-freedom pontoons. *Energy* 209, 118463 (2020)
33. Shi, J., et al.: A 39-year high resolution wave hindcast for the Chinese coast: Model validation and wave climate analysis. *Ocean Eng.* 183, 224–235 (2019)
34. Mansard, E.P.D., Funke, E.R.: The measurement of incident and reflected spectra using a least squares method. In: *Proceedings of the 17th International Conference on Coastal Engineering (ICCE)*. Sydney, Australia (1980)
35. Peng, W., et al.: Numerical simulation of interactions between water waves and inclined-moored submerged floating breakwaters. *Coastal Eng.* 82, 76–87 (2013)
36. Wei, Y., et al.: Wave interaction with an oscillating wave surge converter. Part II: Slamming. *Ocean Eng.* 113, 319–334 (2016)
37. Renzi, E., Wei, Y., Dias, F.: The pressure impulse of wave slamming on an oscillating wave energy converter. *J. Fluids Struct.* 82, 258–271 (2018)
38. Peng, W., et al.: Wave tank experiments on the power capture of a float-type wave energy device with a breakwater. *J. Renewable Sustainable Energy* 10(5), 054501 (2018)
39. Drimer, N., Agnon, Y., Stiassnie, M.: A simplified analytical model for a floating breakwater in water of finite depth. *Appl. Ocean Res.* 14(1), 33–41 (1992)
40. Greaves, D., Iglesias, G., *Wave and Tidal Energy*, John Wiley & Sons, Hoboken, NJ (2018)
41. Liu, Z., et al.: Study on energy conversion and storage system for a prototype buoys-array wave energy converter. *Energy Sustainable Dev.* 34, 100–110 (2016)
42. Wang, R.-q., et al.: Nonlinear and viscous effects on the hydrodynamic performance of a fixed owc wave energy converter. *Coastal Eng.* 131, 42–50 (2018)
43. Zhang, H.M., et al.: Hydrodynamic performance of a dual-floater hybrid system combining a floating breakwater and an oscillating-buoy type wave energy converter. *Appl. Energy* 259, 114212 (2020)
44. Zhang, Y., Zou, Q.-P., Greaves, D.: Air–water two-phase flow modelling of hydrodynamic performance of an oscillating water column device. *Renewable Energy* 41, 159–170 (2012)
45. Peng, W., et al.: Experimental and numerical study on hydrodynamic performance of a wave energy converter using wave-induced motion of floating body. *J. Renewable Sustainable Energy* 7, 053106 (2015)
46. Nguyen, H.N., Tona, P.: An efficiency-aware continuous adaptive proportional-integral velocity-feedback control for wave energy converters. *Renewable Energy* 146, 1596–1608 (2020)

How to cite this article: Peng, W., et al.: Experimental investigation of a triple pontoon wave energy converter and breakwater hybrid system. *IET Renew. Power Gener.* 15, 3151–3164 (2021).
<https://doi.org/10.1049/rpg2.12214>